Noname manuscript No.
(will be inserted by the editor)

The optical performance of the PILOT instrument from ground end-to-end tests

R. Misawa, J-Ph. Bernard, Y. Longval, I. Ristorcelli, P. Ade, D. Alina, Y. André, J. Aumont, L. Bautista, P. de Bernardis, O. Boulade, F. Bousqet, M. Bouzit, V. Buttice, A. Caillat, M. Chaigneau, M. Charra, B. Crane, F. Douchin, E. Doumayrou, J.P. Dubois, C. Engel, M. Griffin, G. Foenard, S. Grabarnik, P. Hargrave, A. Hughes, R. Laureijs, B. Leriche, S. Maestre, B. Maffei, C. Marty, W. Marty, S. Masi, J. Montel, L. Montier, B. Mot, J. Narbonne, F. Pajot, E. Pérot, J. Pimentao, G. Pisano, N. Ponthieu, L. Rodriguez, G. Roudil, M. Salatino, G. Savini, O. Simonella, M. Saccoccio, J. Tauber, C. Tucker

Received: date / Accepted: date

Abstract The Polarized Instrument for Long-wavelength Observation of the Tenuous interstellar medium (*PILOT*) is a balloon-borne astronomy experiment designed to study the linear polarization of thermal dust emission in two photometric bands centred at wavelengths 240 μm (1.2 THz) and 550 μm (545 GHz), with an angular resolution of a few arcminutes.

Several end-to-end tests of the instrument were performed on the ground between 2012 and 2014, in order to prepare for the first scientific flight of the experiment that took place in September 2015 from Timmins, Ontario, Canada. This paper presents the results of those tests, focussing on an evaluation of the instrument's optical performance. We quantify image quality across the extent of the focal plane, and describe the tests that we conducted to determine the focal plane geometry, the optimal focus position, and sources of internal straylight. We present estimates of the detector response, obtained using an internal calibration source, and estimates of the background intensity and background polarization.

Keywords Far Infrared · Interstellar Dust · Optics · PILOT · Point Spread Function · Polarization · Straylight

R. Misawa , J-Ph. Bernard, G. Foenard, A. Hughes, C. Marty, W. Marty, L. Montier, B. Mot, J. Narbonne, I. Ristorcelli, G. Roudil
Institut de Recherche en Astrophysique et Planetologie (IRAP), Université Paul Sabatier, 9 Av du Colonel Roche, BP 4346, 31028 Toulouse cedex 4;
E-mail: Ruka.Misawa@irap.omp.eu

C. Engel
LAM 38 rue F. Joliot-Curie 13388 Marseille CEDEX 13, France;

J. Aumont, A. Caillat, M. Chaigneau, M. Bouzit, V. Buttice, M. Charra, B. Crane, J.P. Dubois, B. Leriche, Y. Longval, B. Maffei, F. Pajot
Institut d'Astrophysique Spatiale (IAS), Bât 121, Université Paris XI, Orsay, France;

P. Ade, M. Griffin, P. Hargrave, G. Pisano, C. Tucker
Department of Physics and Astrophysics, PO BOX 913, Cardiff University, 5 the Parade, Cardiff, UK;

Y. André, L. Bautista, F. Bousqet, F. Douchin, S. Maestre, J. Montel, O. Simonella, M. Saccoccio
Centre National d'Études Spatiales, DCT/BL/NB, 18 Av. E. Belin, 31401 Toulouse, France;

P. de Bernardis, S. Masi, M. Salatino, J. Pimentao
Universita degli studi di Roma "La Sapienza", Dipartimento di Fisica, P.le A. Moro, 2, 00185, Roma, Italia;

O. Boulade, E. Doumayrou, L. Rodriguez
CEA/Saclay, 91191 Gif-sur-Yvette Cedex, France;

S. Grabarnik, R. Laureijs, J. Tauber
Scientific Support Office, SRE-S, ESTEC, PO Box 299,2200AG Noordwijk, The Netherlands;

N. Ponthieu
Grenoble University, Grenoble, France;

E. Pérot
Thales Services, Toulouse, France;

G. Savini
Optical Science Laboratory, UCL, Gower St. WC1E 6BT London, UK;

D. Alina
Department of Physics, School of Science and Technology, Nazarbayev University, Astana 010000, Kazakhstan;

1 Introduction

The interstellar medium (ISM) consists mainly of gas (99% by mass) and dust (1% by mass) at very low densities. Interstellar dust grains play a crucial role in molecule formation, photo-electric heating of neutral interstellar gas, and cooling in dense star-forming regions. Emission from dust in the Milky Way and external galaxies is a foreground contaminant of the Cosmic Microwave Background (CMB) signal. In addition, dust emission is widely used to trace ISM structure in the local Universe (e.g. [1–3]), and to estimate the mass of galaxies at high redshift (e.g. [4]).

In the infrared-to-submillimetre regime, thermal dust emission is typically modelled using a modified blackbody spectrum. The largest ISM dust grains are primarily heated by photons in the ultraviolet-optical regime, reaching an equilibrium temperature of $T_D \simeq 17\,\mathrm{K}$ in the diffuse ISM (e.g. [5]). The peak of their emission occurs around $150\,\mu\mathrm{m}$. The properties of the ISM dust grains as revealed by the variations of the emission spectral energy distribution (SED) have been well studied using recent data from the *Herschel* [6] and *Planck* [7] satellites.

Thermal dust emission is polarised, due to the elongated shape of dust grains and the statistical alignment between the short axis of dust grains and the magnetic field that pervades the ISM. Since the re-radiation of absorbed starlight by a dust grain occurs preferentially along the long axis of the grain, this produces emission that is polarized perpendicular to the magnetic field lines. For the same reason, non-polarised starlight passing through aligned dust grains also becomes polarized: preferential absorption along the grain's long axis leads to extinction that is polarized parallel to the magnetic field lines. In our Galaxy, the magnetic field is preferentially oriented in the plane of the disk. Therefore, the observed polarization of stellar extinction is mostly parallel to the plane, and dust emission is polarized mostly orthogonal to the plane.

Historically, the measurement of polarised emission in the far-infrared (FIR) has been severely hampered by atmospheric absorption. Ground-based observations are mostly limited to bright emission in star-forming regions (e.g. [8]), where they have been used to probe the direction of the magnetic field, which likely plays a central role in regulating the star formation process. In those regions, the polarization levels are low (a few %). The balloon-borne experiment Archeops measured dust polarisation at $850\,\mu\mathrm{m}$ (353 GHz) over a fraction of the Galactic plane ([9]), with much higher sensitivity than ground measurements. These measurements indicated high polarization levels (up to 15%) in the diffuse ISM. Recently, the Planck satellite measured polarisation in the wavelength range from $850\,\mu\mathrm{m}$ (353 GHz) to 1.0 cm (30 GHz) with high accuracy, and confirmed the existence of highly polarized regions at high galactic latitudes with polarization fractions up to 20% (see [10]).

Table 1 Main optical characteristics of the *PILOT* instrument.

Field of View	$1^\circ \times 0.76^\circ$
Equivalent Focal Length	1790 mm
Focal Ratio	F/2.6
Photometric Band	$240\,\mu\mathrm{m}$ (1.2 THz)
	$550\,\mu\mathrm{m}$ (545 GHz)
Photometric Band Width	$69.5\,\mu\mathrm{m}$ at $240\,\mu\mathrm{m}$
	$186.2\,\mu\mathrm{m}$ at $550\,\mu\mathrm{m}$
Angular Resolution	$1.44'$ at $240\,\mu\mathrm{m}$
	$3.29'$ at $550\,\mu\mathrm{m}$
Sensitivity	[0.98-6.28] MJy/sr at $240\,\mu\mathrm{m}$
(3-σ in $3.5'$)	[0.33-2.13] MJy/sr at $550\,\mu\mathrm{m}$
Telescope Type	Gregorian
M1 Diameter	0.83×0.81 m
Detector Temperature	~ 300 mK
Total Mass	$\sim$1 ton
Flight Duration	$\sim$24 h

The *PILOT*[1] instrument is designed to obtain wide-field maps of dust polarization in the diffuse ISM at FIR wavelengths. As a consequence, the polarization performance of the complete optical train has to be extremely well-understood and controlled. This performance must be characterized over the entirety of *PILOT*'s large instantaneous field of view of $0.8^\circ \times 1^\circ$, taking into account the possible presence of large thermal variations of the mechanical structure during the flight, and changes of the instrument orientation with respect to gravity during the elevation changes of the instrument. To achieve this, we carried out end-to-end ground tests of the *PILOT* instrument at Centre National d'Études Spatiales (CNES) in Toulouse, in October 2013 and February 2014.

This paper presents the results of the *PILOT* end-to-end ground tests. We briefly describe the instrument in Sect. 2 and the test setup in Sect. 3. The results of calibration tests to measure the instrumental background and its polarization are given in Sect. 4. We discuss measurements to characterize the instrument's internal calibration source in Sect. 5. Results for the quality of the optics, the determination of the focal plane geometry and the internal straylight are given in Sect. 6, Sect. 7 and Sect. 8 respectively .

2 Instrument description

The *PILOT* instrument is described in detail in [11]. Here we only provide a brief description for completeness. The main characteristics of the *PILOT* instrument are given in Table 1. *PILOT* uses a 0.83 m diameter off-axis paraboloid primary mirror (M1) combined with a cryogenically cooled off-axis ellipsoid secondary mirror (M2) in the Mizuguchi–Dragone configuration in order to minimize depolarization

[1] http://pilot.irap.omp.eu

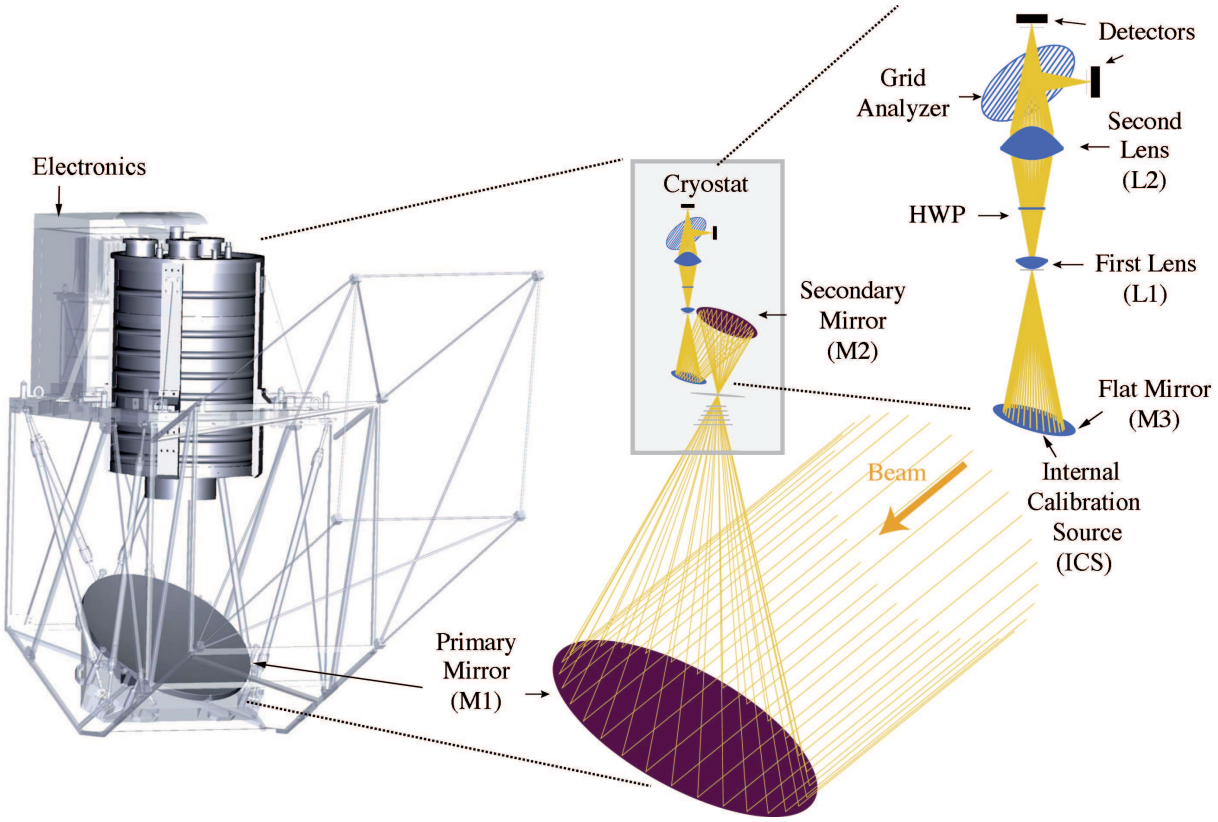

Fig. 1 Schematic diagram of the *PILOT* optics. The cold optics inside the cryostat is maintained at ≃2-4 K. The detectors operate at a temperature of 300 mK.

effects (see Fig. 1 and [12], [13]). Apart from M1, the rest of the optics is cooled to ≃2-4 K, in order to reduce thermal emission from the instrument. The Gregorian telescope composed of M1 and M2 is followed by a re-imager and polarimeter through a flat mirror (M3), which folds the beam and reduces the photometer volume. The L1 and L2 lenses make a telecentric re-imager. The L1 lens images the aperture of M1 onto the Lyot stop, and the L2 lens images the focal plane of the telescope onto the detectors.

The Half-Wave Plate (HWP) is located next to the Lyot stop. A metal grid analyser, inclined 45° with respect to the optical axis, is located in front of the detectors. The HWP is made of Sapphire, a birefringent material that introduces a half-wave phase delay between the two polarizations of the incident light. The polarization analyzer consists of parallel metallic wires which transmit one polarization to the transmission arrays (TRANS) and reflect the other polarization onto the reflection (REFLEX) arrays. Observations at at least two different HWP angles are required to measure the three Stokes parameters I,Q,U.

The detector blocks and readout equipment were developed by CEA/LETI as spare modules from the PACS instrument on board the Herschel satellite (for more detail, see [14]). The detector blocks consists of 2048 individual bolometers (16 × 16 pixels × 8 arrays) cooled to 300 mK by a closed cycle ^{3}He fridge. The optical system is designed to work simultaneously in two broad photometric bands, centered at 240 μm (1.2 THz) and 550 μm (545 GHz), with a 30% bandwidth. However, for the first flight of *PILOT*, the whole focal plane was configured to operate at 240 μm. The angular resolution of the system is set by a Lyot stop located in a pupil plane next to the HWP and is a few arcminutes at 240 μm. Individual bolometers operate without a collecting horn and are 750 μm on the side, which corresponds to 1.4′ on the sky.

An Internal Calibration Source (ICS) is located behind the M3 mirror, and can be used to illuminate the detectors with stable, modulated light. This source is highly reproducible, permitting measurements of variations of the response flat-field. The ICS is the spare of the PCAL calibration source of Hershel/SPIRE and is driven in current with a square modulation (see details in Sect. 5). In *PILOT*'s nominal observing mode, calibration sequences are performed at the beginning and the end of each science scan.

The pointed instrument, composed of the primary mirror M1 and the photometer both housed within an aluminium hexapod, is installed in the gondola. The gondola is made of aluminium bars and connecting spheres. The total weight of the experiment is approximately 1 tonne. The gondola is

designed to fly at an altitude of 40 km (4 hPa pressure) in the stratosphere.

The equivalent focal length of the *PILOT* optical system is 1.8 m and the numerical aperture is F/2.5. The diffraction limit of the system is $1.44'$. In order to preserve the image quality, the mechanical accuracy between the primary mirror and the detectors must controlled to within 0.6 mm, $3.6'$ and 0.06° in translation, offset/tilt and rotation respectively (e.g. [13]).

2.1 Measurement of Polarization

For the *PILOT* instrument, the equations relating measurements m to polarization fraction p and angle ψ can be written (see details in [15, 11])

$$m = R_{xy}T_{xy}I \times [1 \pm \frac{1+2\gamma}{2} p\cos 2\psi + (p\beta\cos 2\psi \pm \beta)\cos 2\omega + p\beta \sin 2\psi \sin 2\omega \pm \frac{1-2\gamma}{2} p\cos 2\psi \cos 4\omega \pm \frac{1-2\gamma}{2} p\sin 2\psi \sin 4\omega] + O_{xy} \quad (1)$$

where I is the total intensity, R_{xy} is the detector response, T_{xy} is the optics transmission, β is the differential transmission between the fast and slow axis of the HWP and γ is the phase shift induced by the HWP. Positive terms in the above equation correspond to measurements on the TRANS arrays; negative terms correspond to the and REFLEX arrays. The additional term O_{xy} accounts for a an arbitrary electrical offset and the instrumental background. For an ideal HWP ($\beta = 0$ and $\gamma = -0.5$), Eq. 1 simplifies to

$$m = R_{xy}T_{xy}I \times [1 \pm p\cos 2\psi \cos 4\omega \pm p\sin 2\psi sin4\omega] + O_{xy}. \quad (2)$$

3 Equipment setup for end-to-end calibration tests

The end-to-end tests were performed in a temperature- and humidity- controlled clean room at CNES in Toulouse. During these tests, some arrays showed temporary connection problems that affected the multiplexing of individual bolometers. As a consequence, for most of the test results presented here, results for arrays# 1, 3 and 5 are not shown.

A schematic view of the equipment used in the end-to-end test is shown in Figure 2. The *PILOT* instrument, composed of the photometer and M1 primary mirror, is placed in front of a 1 m diameter Newtonian collimator with a focal length of 5.34 m, mounted on a 6 m height tower. This set-up allows us to illuminate the full surface of M1 with unpolarized parallel light, simulating a point source at infinite distance. The collimator source is a 100 W high-pressure mercury arc lamp, with a 10 mm diameter bulb in a quartz envelope. It is located behind a 2 mm diameter hole mounted on a triaxial motorized system, which can move the source at the focus of the collimator. The source is modulated by a rotating chopper.

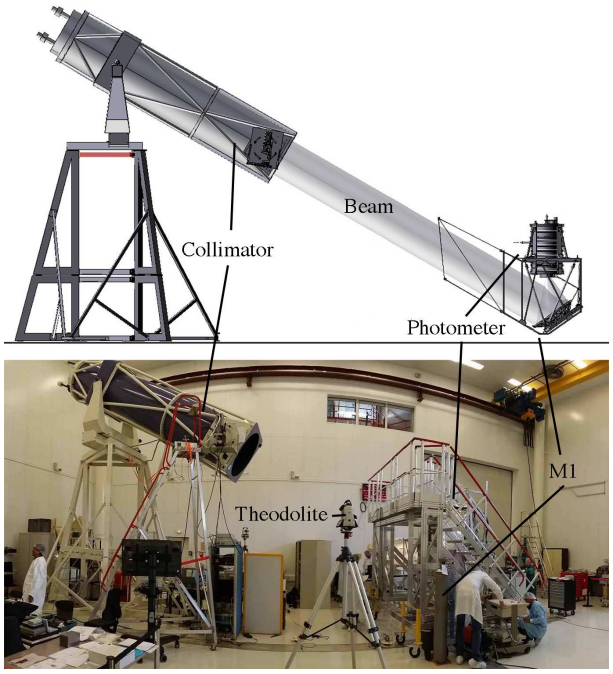

Fig. 2 Equipment used during *PILOT* end-to-end calibration tests. Upper: schematic view of the test equipment, bottom: installation in the integration room at CNES. On the left is a 1 m diameter collimator and on the right is the *PILOT* integrated instrument. The collimator simulates a point source at infinite distance.

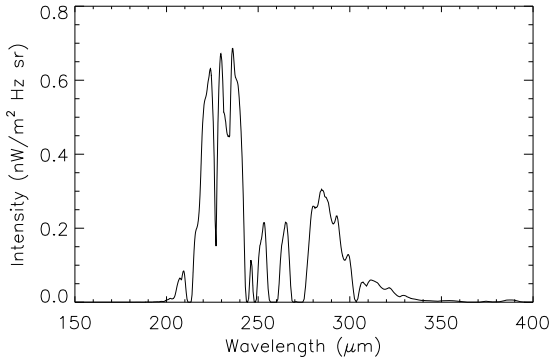

Fig. 3 Expected spectrum of the incident collimator light in the *PILOT* 240 μm band (see text for details).

The expected spectrum of the incident light is shown in Fig. 3. This spectrum assumes that the collimator source is a blackbody with temperature of 1800 K, and takes account of the reflectivity of the primary and the secondary mirrors of the collimator and the atmospheric absorption in the test room for an average room temperature 23.0° C and average humidity of 47.9%. The atmospheric absorption was modelled with the MODTRAN 5.3 software [16], using the summer mid-latitude atmospheric model.

We co-aligned the *PILOT* instrument and the collimator with theodolites and a laser-tracker with $\sim 2''$ accuracy. Under ground test conditions, the total background is dominated by emission from the 300 K environment and is much larger than in flight. The background level was estimated through a photometric model (see [17]). Based on these calculations, an optical attenuator that reduces the background radiation by a factor of about 20 was constructed. This attenuator was inserted on the 3 K screen of the cryostat during the ground tests, in order to bring the background level on the detectors closer to the expected in-flight value of about 4.5 pW/pix at the center of the focal plane.

4 Background level and polarization

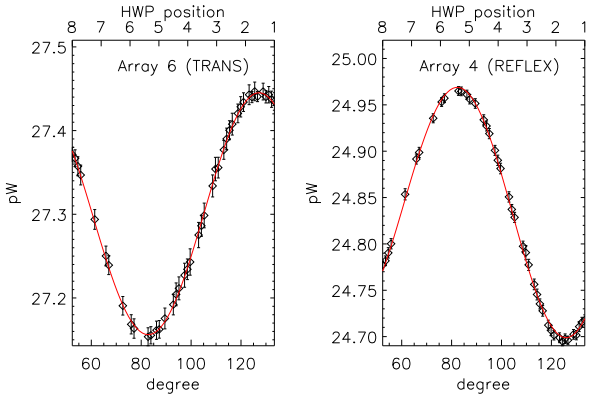

Fig. 4 Average signal on TRANS array# 6 and corresponding REFLEX array# 4 when the HWP rotates from 52.37° to 133.37° (HWP position# 0.9-8.1).

In this section, we describe the tests that we conducted in order to assess the background level and its spatial distribution on the focal plane. For this purpose, we removed M1 and placed an eccosorb layer in front of the photometer. We performed tests with the eccosorb at room temperature (300 K), and immersed in liquid nitrogen at 77 K. In both cases, the system holding the eccosorb was connected to the entrance window of the photometer via a plastic tent filled with nitrogen atmosphere with humidity less than 2 % to reduce absorption. The distance between the eccosorb and the entrance window is 140 ± 10 cm. In this configuration, the photometric model described in [11] predicts that the total background is dominated by the eccosorb emission. Measurements were obtained at several positions of the HWP.

Figure 4 shows the average signal over array# 6 of the TRANS focal plane and over the corresponding array# 4 of the REFLEX focal plane as a function of the HWP position. It can be seen that the signal strongly varies with the HWP position in phase opposition on both focal planes. In principle, the variations observed could either be due to an imperfection of the HWP, such as a different transmission for orthogonal polarizations, or to a true polarization of the background. Against the former interpretation, we observed that the signal of the ICS does not show a modulation with HWP position. We also observed that the apparent direction of polarization of the background signal changes when a reflecting mirror is inserted just in front of the cryostat window. This indicates that the origin of the modulation observed is likely due to a true polarization of the background light. The exact origin of this polarization is currently unclear. In principle, it could be caused by the polarized emission of some of the optical components along the optical path, such as, for instance, the entrance window of the cryostat. However, in the ground configuration, the background is largely dominated by emission from the air in the room and the contributions of such optical elements is $< 5\%$ of the total background. Their polarized emission therefore cannot explain most of the polarization observed and we believe that the observed polarization is likely induced by propagation of unpolarized signal in the optics. Despite the fact that the optical configuration is optimized to minimize instrumental polarization for sources outside the optical system, most of the background is contributed by optical elements located between M1 and M2, and is therefore not compensated completely by the Mizuguchi–Dragone configuration of the optics. The observed signal is maximum on the TRANS array (and minimum on the REFLEX arrays) between positions 1 and 2 of the HWP, which corresponds to an angle of about 11.25° between the fast axis of the HWP with respect to vertical. Since the polarizer wires are parallel to the vertical direction, the signal variations with the HWP position suggest that the polarization direction of the background is roughly orthogonal to the vertical axis in this configuration.

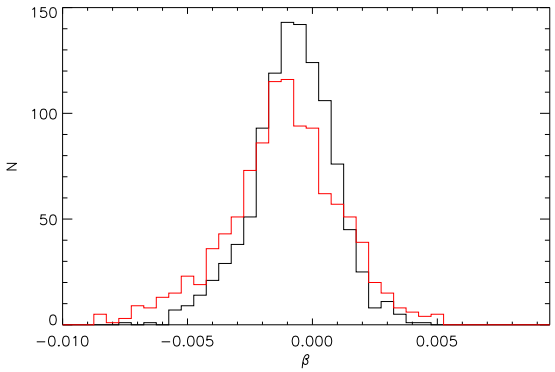

Fig. 5 Histogram of the differential transmission between the fast and slow axis of the HWP, β. The fact that the distribution is centered around $\beta \sim 0$ indicates that the HWP is close to perfect. The black and red lines are for data in front of a 77 K and a 300 K background respectively.

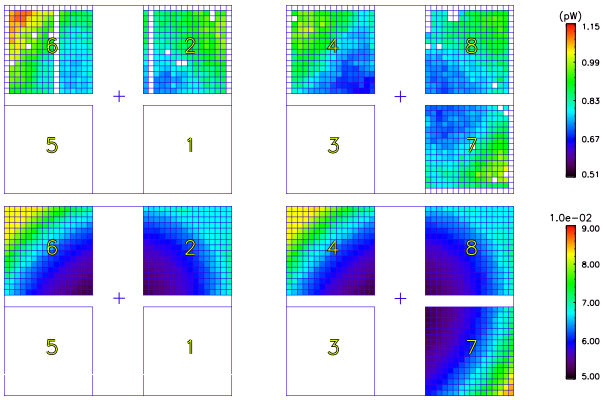

Fig. 6 Top: Spatial distribution of the background as derived from differential measurements between backgrounds at 77 K and 300 K. The scale shown corresponds to the 300 K eccosorb background. Bottom: Spatial distribution of the instrument transmission as simulated using the Zemax software. The unit is arbitrary.

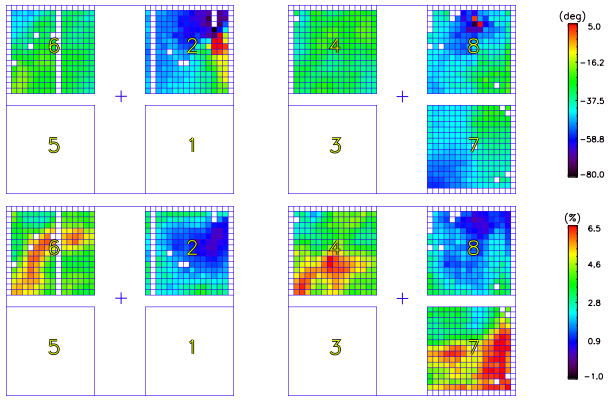

Fig. 8 Spatial distribution of the polarization angle ψ (top) and polarization fraction p (bottom) as derived from fitting the data using Eq. 2.

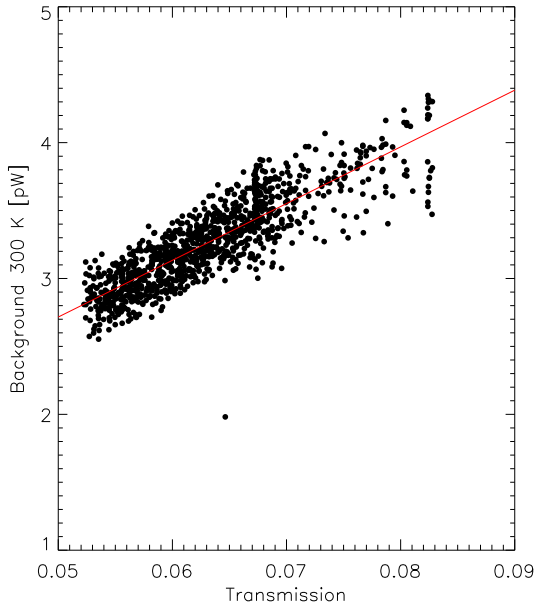

Fig. 7 Correlation between the instrument transmission and the 300 K background signal. The line shows the best linear fit: $S_{xy} = 41.7 \times T_{xy} + 0.629$.

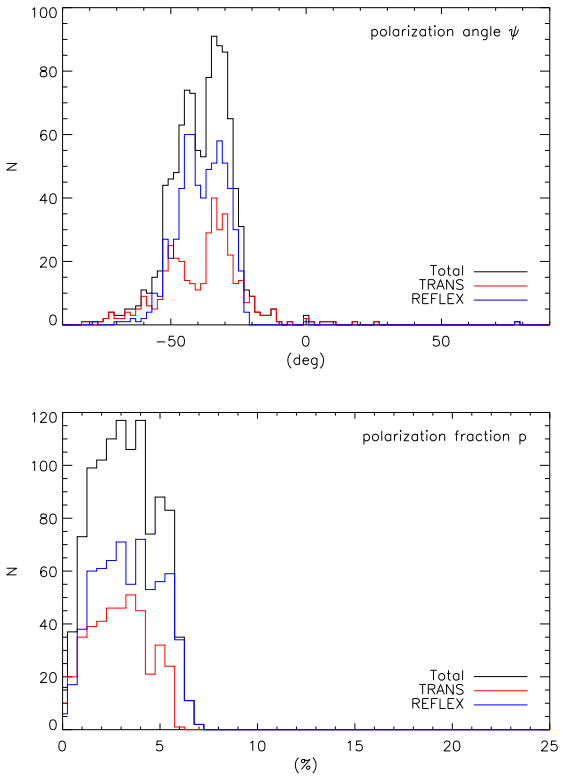

Fig. 9 Histograms of the polarization angle ψ (top) and the polarization fraction p (bottom) corresponding to Fig. 8. The black, red and blue lines show the curves computed for all pixels and the TRANS and REFLEX pixels respectively. The polarization angle ψ is distributed between -60° and -20° and the polarization fraction p is distributed between 0 and 7 %.

In order to measure β, we fit Eq. 1 to the signal of all bolometers of both focal planes, assuming $\gamma = -0.5$ (see Sec. 6.3). Figure 5 shows the distributions derived for β. A Gaussian fit to these distributions yields an average $\beta = -0.0004 \pm 0.0016$. This β value indicates that there is no strong evidence for differential transmission between the fast and slow axes of the HWP.

From Eq. 2, and assuming that the background sources at 300 K and 77 K have a flat spatial distribution and the same polarization fraction and angle, the difference between measurements in front of the 300 K and the 77 K background sources can be written as below:

$$m_{300K} - m_{77K} = R_{xy} T_{xy} (I_{300K} - I_{77K}), \quad (3)$$

where I_{300K} and I_{77K} are the intensity of the 300 K and the 77 K background sources, respectively. Note that the contribution to the instrumental background from the instrument

itself and the electrical offset cancel. In turn, a map of the instrument transmission can be derived from this difference, as

$$T_{xy} = \frac{m_{300K} - m_{77K}}{R_{xy}(I_{300K} - I_{77K})}. \quad (4)$$

Since the fraction of the total signal produced by the instrument is small compared to that from the eccosorb dominating the background, the background map itself can be estimated as

$$S_{xy} = BR_{xy}T_{xy}I_{300K}, \quad (5)$$

or, replacing T_{xy} from Eq. 4,

$$S_{xy} = \frac{m_{300K} - m_{77K}}{R_{xy}} \times \frac{I_{300K}}{I_{300K} - I_{77K}}. \quad (6)$$

Figure 6 shows the spatial distribution of S_{xy} computed using Eq. 6. To obtain these maps, we use the detector response maps R_{xy} measured from detector calibrations in front of an extended black body at known temperature and assuming emission in the Rayleigh-Jeans regime ($I \propto T$). The median background levels derived are 0.83 pW/pix and 3.24 pW/pix for the background produced by the 77 K and 300 K eccosorb, respectively. The background distribution shows smaller values towards the center of the focal plane and higher values towards the edges. Figure 6 also shows the spatial distribution of the total transmission of the instrument computed using the Zemax software. The lower transmission values near the center of the focal plane are due to the presence of lens L2. The measured and simulated distributions are in reasonable agreement, indicating that the observed shape of the background illumination is set by the absorption by lens L2. Figure 7 shows the correlation between the 300 K background intensity and the instrument transmission. A least-squares fit is indicated by the blue line. The best correlation between these quantities is obtained for a transmission map shifted by -6.5′ in cross-elevation and -4.1′ in elevation. These offsets can be understood as a small shift between the center of the focal plane as defined by the focal plane geometry (see Sect. 7) and the optical axis of the cold optics inside the cryostat.

According to the predictions of our photometric model in the ground calibration configuration, the 300 K eccosorb emission should contribute a background level of 3.18 pW/pix (see [11]). This value agrees well with the measured value measured of 3.24 pW/pix.

Figure 8 shows the spatial distribution of the polarization angle ψ and polarization fraction p derived from fitting the background intensity variations with HWP position, using Eq. 2. The fit was performed independently for the TRANS and REFLEX focal planes which observe the same direction. As a consequence, the spatial distribution of the polarization angle is similar on the two focal planes. Differences in the polarization fraction between the two focal planes likely originate from uncertainties in deriving the background value. Figure 9 shows that the polarization angle ψ is distributed between -60° and -20° , and the polarization fraction p varies between between 0 and 7 %.

5 Internal calibration source

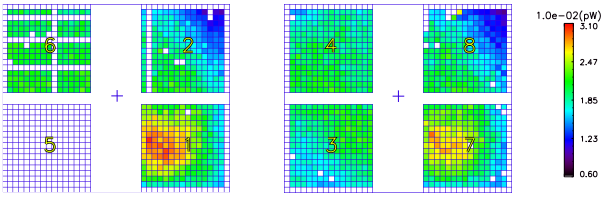

Fig. 10 Map of ICS illumination in pW/pix for an ICS current I_{ICS} =1.3 mA. For each focal plane, the illumination shape is an oval centered on the optical axis, with its short axis roughly parallel to the elevation direction.

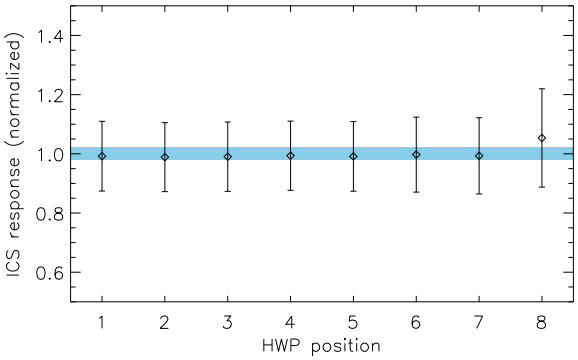

Fig. 11 ICS response as a function of the HWP position. Each data point shows the average ICS response over a whole array. The error bar for each HWP position represents the ± 1-σ time variations of ICS response during 4.3 hours of observations while the focal plane temperature was stable. The blue region shows the corresponding ±1-σ uncertainty of ±2.2 %.

The *PILOT* Internal Calibration Source ICS is an electrically heated submillimeter source, which is used for calibration at the end of observing scans. The current in the source is modulated by a square wave function and its intensity is such that the ICS illumination is sufficient for calibration, but low enough so that the ICS light produces no significant increase of the total background on the detectors. Figure 10 shows the spatial distribution of the ICS signal on the focal plane. The ICS illumination shape is an oval with its short axis roughly parallel to the elevation direction. Measurements performed at various current intensities across the ICS show that the signal on detectors is proportional to the

electrical power dissipated in the ICS. The ICS illumination at the field edges is about two times lower than the peak intensity. The normalized ICS response S_{ICS}/P_{ICS} varies by only about 2.2 % as a function of the HWP position as shown in Fig. 11. In this figure, the error bar for each HWP position represents the ± 1-σ time variations of ICS response during 4.3 hours of observations while the focal plane temperature was stable. The plot shows that the response of the system to the ICS illumination is almost constant with the HWP position. Similarly, no variation in the shape of the ICS illumination with HWP position was observed.

The median illumination of the ICS is ~ 0.02 pW/pix for I_{ICS} =1.3 mA (Fig. 10). This is $\simeq 200$ times lower than the expected in-flight background level (see Fig. 6). This is compatible with the requirement that the ICS source does not modify the optimal operating regime of the bolometers.

6 Focus and image quality

6.1 Defocus

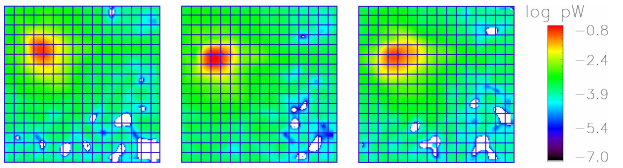

Fig. 12 PSF shape for different focus positions at $Z = -1.7$, 0.2 and 1.7 mm respectively from left to right, for array# 7. Z =0.2 corresponds to the best focus position. The other PSF images obtained with $Z = -1.7$ and 1.7 are clearly more elongated.

Table 2 Best focus positions derived for each array.

Array	X [mm]	Y [mm]	Z [mm]
2	0.0	0.0	0.2
4	0.0	0.0	0.0
6	0.0	0.0	0.2
7	0.4	-0.8	0.2
8	-	-0.4	0.2

In order to derive the best position of M1 with respect to the photometer, we performed a series of measurements at various focus positions along three orthogonal axes (X, Y, Z), around the best focus position predicted by optical modelling. The Z axis corresponds to the optical axis of the photometer. For each position of the mirror, the collimator source was positioned at a limited number of locations in the focal plane, and images of the source were obtained.

To estimate the impact of defocussing on *PILOT*'s optical performance, all three axes of the focal plane have been explored using offsets of ± 0.8 mm along the X and Y axis, and ± 1.6 mm along the Z axis. Figure 12 shows three images at different positions $Z = -1.7$, 0.2 and 1.7 mm from the predicted best focus position for a source illuminating the same position on array# 7. The Point Spread Function (PSF) obtained at $Z = -1.7$ and 1.7 are elongated towards the upper left and upper right respectively, which is likely due to astigmatism. The PSF for the best position of M1 ($Z = 0.2$) is the sharpest and the roundest. The Full Width Half Maximum (FWHM) and encircled energy of the PSF as a function of defocusing distance were derived by fitting the obtained images with a 2D-Gaussian function. The best focus position was determined as the position of minimum FWHM. Figure 13 shows the FWHM of the observed source on array# 2 at several defocusing distances along X, Y and Z axis. The best focus position for each array is summarized in Tab. 2. Overall, we find that the optimal focus position for M1 is at X=0.0 mm, Y=0.0 mm and Z=0.2 mm from the best position predicted by our optical model. The data obtained on array# 8 along the X axis were not sufficient to allow reliable determination of the best position.

The tolerance of M1 is ± 0.6 mm if the position of M2 is accurate (see Fig. 13). The size of FWHM changes by up to $0.25'$ for focus offsets along the X and Y axis within the tolerance of M1 and by up to $0.4'$ for focus offsets along the Z axis. These results indicate that the acceptable region around the best focus position is larger than predicted. Fig. 14 shows the variation of the PSF within the focal plane, at the best focus position. The apparent elongations of the PSF visible in the horizontal and vertical directions are likely to be due to diffraction from the support structure of the secondary mirror of the collimator used to produce the source. The figure also shows distortions of the PSF near the edges of the focal plane, which are attributed to reflected light by the field stop of the instrument.

6.2 Point spread function

In order to obtain accurate measurements of the instrument Point Spread Function (PSF) and to check the image quality of the instrument, we used a microscan technique where the collimator point source is moved in the focal plane with steps much smaller ($1/10^{th}$) than the pixel size. Individual images obtained at each step are shifted by the source displacement, as given by the control system. They are then co-added to produce a well-sampled PSF. These measurements were obtained at the best focus position of M1 as determined in Sect. 6.1.

We computed the shape of the expected diffraction-limited PSF using the Zemax software, taking into account the effect of the collimator, secondary mirror holding structure

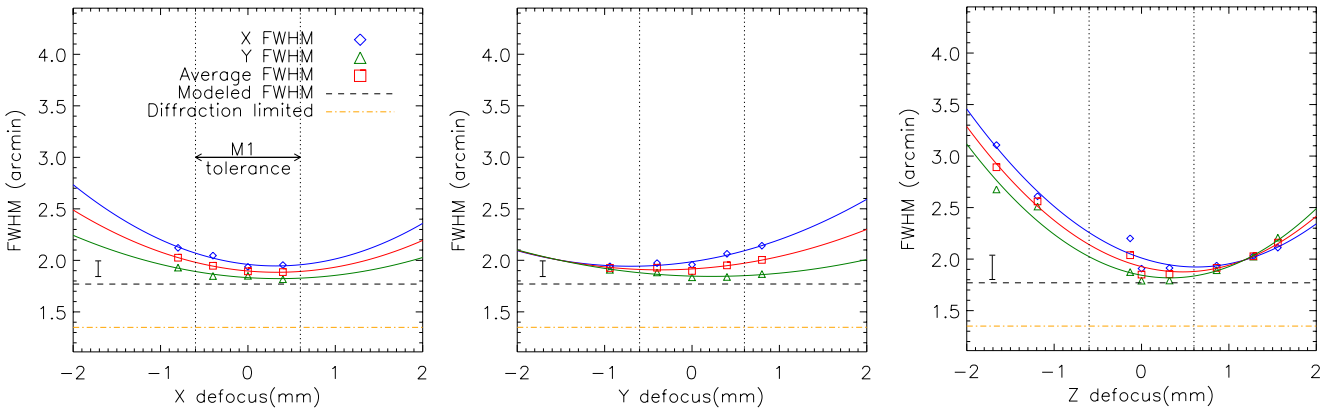

Fig. 13 The PSF FWHM values derived from measurements on array# 2 as a function of focus offsets along the X (right), Y (center), and Z (left) axis. The FWHM in the x-direction on the array is shown in blue, the FWHM in the y-direction in green, and the average FWHM in red. The horizontal lines show the diffraction limit (dash-dotted), and the Zemax simulated FWHM values (dashed). The region between the dotted vertical lines is within the tolerance of M1. The error bar shown the dispersion of FHWM measured across arrays at the best focus position.

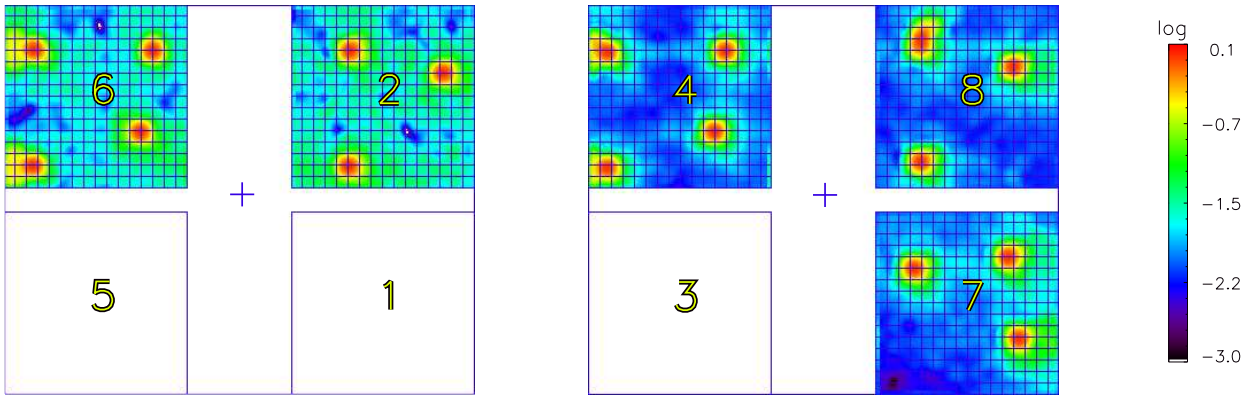

Fig. 14 Composite images showing the normalized PSF at various positions in the focal plane, for the focus position corresponding to X=0, Y=0, and Z=0.2 mm.

and the diameter of the source diaphragm. This simulated PSF was computed at a single wavelength of 250 μm. We also predicted the signal for each source position of the microscan, by positioning the simulated PSF at the location of the source on the array and integrating its flux in the pixels. These simulated images were treated in the same way as the data in order to produce a simulated co-added PSF, directly comparable to the PSF obtained from the actual measurements.

Figure 15 shows the measured and simulated PSF images on pixel (3, 7) of array# 6, and the corresponding horizontal, vertical and ±45° diagonal cuts. The observed PSF is in good agreement with the simulated PSF. The FWHM of the average profile of the simulated PSF is $\simeq 1.75'$ (1.25 pixels). The FWHM of the average profile of the measured PSF is $\simeq 2.0'$ (1.44 pixels). The remaining difference between the observed and simulated FWHM could be due to our simplifying assumption of a single wavelength in the PSF calculation. A low intensity cross pattern around the PSF is observed along the X and Y direction on all PSF images. They are likely due to the diffraction of four struts that are part of structure supporting the secondary mirror of the collimator. These structs are aligned with the pixel direction, which explains why the profile cuts in X and Y are slightly larger than the diagonal cuts.

6.3 Performance of the HWP

Here we evaluate the value of γ, which represents the phase shift induced by the HWP. We set the polarizer located between the collimator and M1 at a given position and derived the source flux by fitting a Gaussian function to the source profile. We applied Eq. 1 to the observed source intensity and derived the values of γ shown in Fig. 16, assuming the β value derived in Sec. 4. We measure $\gamma = -0.53 \pm 0.05$ and $\gamma = -0.49 \pm 0.02$ for the TRANS and REFLEX arrays respectively. These values are in agreement with the ideal value of γ=-0.5. The β and γ values that we obtain indicate

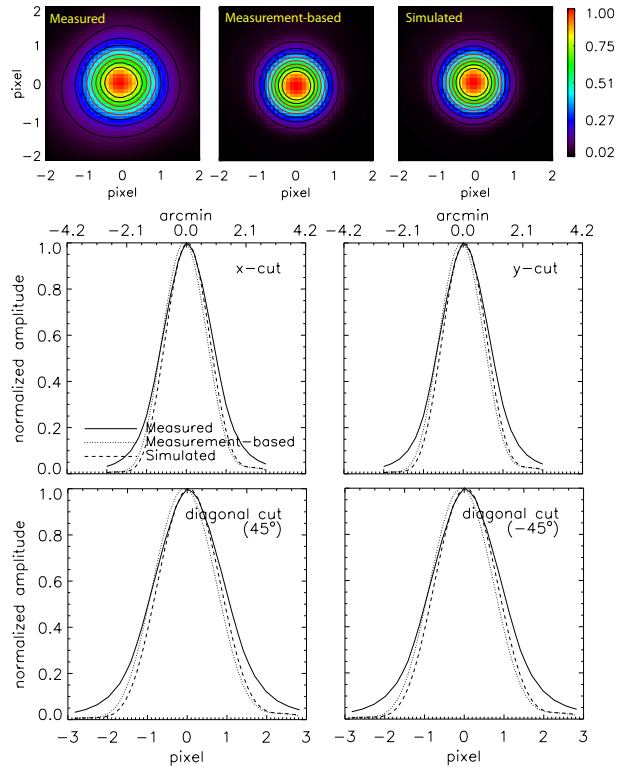

Fig. 15 Top: images of the PSF measured at the best focus position (left), simulated PSF based on measured micro-scanning position (middle), and the simulated single PSF (right). The measured PSF is obtained from a micro-scanning pattern around pixel (3, 7) of array# 6. The simulated single PSF corresponds to the beam at measured position. The amplitude is normalized to the peak intensity. The dimension of the images is 4×4 pixels corresponding to $5.6' \times 5.6'$. The contour levels are in steps of 0.1 between 0.1 and 1.0. Middle and Bottom: profiles of the measured PSF (solid line), the simulated PSF (dashed line) and the measurement-based simulated PSF (dotted line) along the pixel axis and along axis rotated at 45° and -45° .

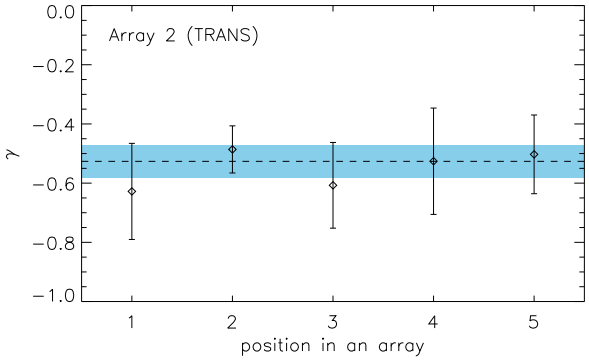

Fig. 16 Variations of γ as a function of the HWP position on array#2 (TRANS). Diamond symbols show the average γ value for each position, the dashed line indicates the average γ value over all positions. The uncertainties at each HWP position show the ± 1-σ on γ as derived from the fit. The blue region shows the corresponding ± 1-σ uncertainty. The γ value for an ideal HWP is -0.5.

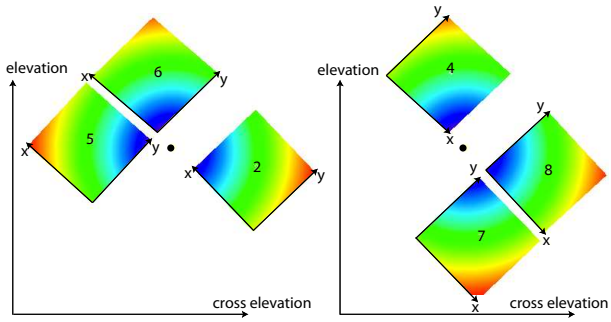

Fig. 17 Image of the *PILOT* focal plane as reconstructed from the measurement of point sources of known directions. The position of the optical axis is shown by the black dot. The cross-elevation and elevation directions are shown for both the TRANS (left) and REFLEX (right) focal planes. The color scale shows the distance to the focal plane center. All images are displayed with a color table going from 0 to $20'$.

that the HWP performs as well as expected and that Eq. 2 applies.

7 Focal plane geometry

We combine the known position of the collimator source and the observed position of the source in the focal plane, in order to constrain the focal plane geometry. The measurements have been obtained at several source elevations, in order to check for possible distortions of the instrument under gravity as the elevation of the optical axis changes.

7.1 Analysis

The collimator beam orientation in azimuth and elevation is known from theodolite measurements, with respect to a fiducial point located near the center of a given array.

We fit the following system of equations:

$$\begin{pmatrix} \Delta_{cel} - \delta^0_{cel} \\ \Delta_{el} - \delta^0_{el} \end{pmatrix} = \begin{pmatrix} \delta_x \\ \delta_y \end{pmatrix} \begin{pmatrix} \cos\alpha & \sin\alpha \\ -\sin\alpha & \cos\alpha \end{pmatrix} \begin{pmatrix} x - x_0 \\ y - y_0 \end{pmatrix} \quad (7)$$

where x and y are the measured pixel position of the peak of the PSFs along the array directions, x_0 and y_0 are the pixel position of the rotation center, α is the rotation angle, and δ_x and δ_y are the pixel scale along the array directions. Δ_{cel} and Δ_{el} are the known cross-elevation and elevation offsets of the collimator source compared to a reference position with respect to the optical axis. δ^0_{cel} and δ^0_{el} are the cross-elevation and elevation offsets between the optical axis and the reference pixel (x_0,y_0).

For each position of the collimator source on the focal plane, we averaged the on-source and off-source images according to the beam chopper information. We fit the resulting difference image with a two-dimensional Gaussian function to recover the peak position of the PSF. These positions

were used to fit the focal plane geometry using Eq. 7. x_0, y_0 are set to be the center of each array, and we leave δ_{cel} and δ_{el}, α, δ^0_{cel} and δ^0_{el} as free parameters. The fit procedure was repeated for each array at each elevation of the source.

7.2 Results

The focal plane geometry parameter values were derived for each array by fitting Eq. 7 to the data at different elevations of the source. Figure 17 shows the reconstructed geometry of the focal plane. Table 3 gives the average parameter values derived for each array. The uncertainties listed in the table are the standard deviation of the free parameters derived from independent measurements taken at the various elevations.

We compared the elevation of the optical axis as measured with the laser tracker, and taking into account the actual position of the source as observed in the focal plane, with the collimator source elevation as measured with a theodolite. The comparison showed that the relation is close to linear, with deviations of the order of only $1'$, which indicates that the flexion of the mechanical system between 20 and 50 degree elevation is of the order or less than $1'$.

8 Straylight

PILOT's optical design has been optimized to reduce internal straylight, which is achieved through anti-reflection coatings and tilting of some of the optical components. However, a small fraction of straylight can remain that needs to be estimated and potentially removed in the data processing when bright sources are observed. Characterizing the internal straylight is therefore necessary.

We find that when the strong collimator point source is positioned on a given array, we detect faint defocussed light at a position symmetrical to the main source with respect to the optical axis. This appears consistent with internal straylight bouncing off a given detector, reflected in the optics and returning to the same focal plane. In order to analyze the straylight radiation, we used the calibration data and the same microscanning method as described in Sect. 7.2, but applying the method to the whole focal plane.

8.0.1 Straylight geometry

To characterize the straylight, we have computed the position of the mid-point between the peak of the collimator source PSF and that of the straylight emission. We fit a Gaussian function to the straylight emission and determine both the peak position of source and its straylight using the microscanning data described in Sect. 6.2. For the remaining straylight calculations, we analyse data for which the uncertainty on the peak positions of the source and of the straylight is less than one pixel.

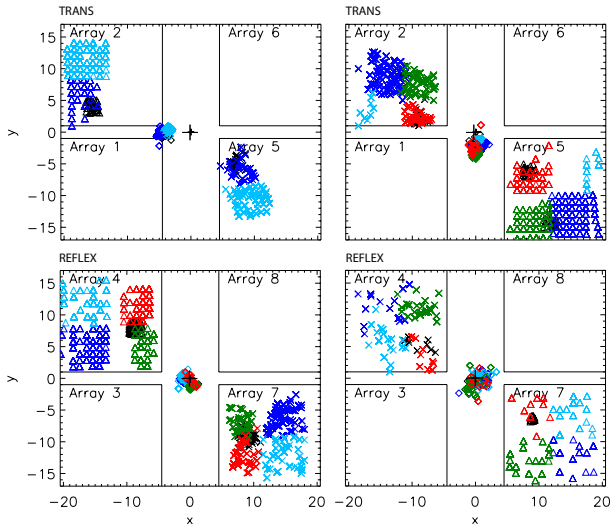

Fig. 18 Distribution of the collimator PSF source peak positions (triangles), straylight peak position (crosses) and the mid-point between the two (diamonds). Red filled circles show the median mid-point of an array. The black plus sign at the center of each focal plane shows the position of the optical axis. Top-left: source on array# 2 and straylight on array# 5. Top-right: source on array# 5 and straylight on array# 2. Bottom-left: source on array# 4 and straylight on array# 7. Bottom-right: source on array# 7 and straylight on array# 4.

Figure 18 shows the distributions of the PSF and straylight peak positions, as well as the mid-point locations. As shown in the figure, the mid-points are clearly seen to concentrate around the focal plane center, on both the TRANS and REFLEX arrays. In particular, the distribution of mid-point positions is consistent with the position of the focal plane center within uncertainties for the REFLEX focal plane (sources and stray-light on arrays# 4 and 7). For the TRANS focal plane, we observe a significant shift of the mid-point positions with respect to the FPC, which appears particularly marked (about 5 pixels) when the source is on array# 2. Unfortunately, it was not possible to confirm this with a PSF centered on the right half of array# 2, due to the presence of a dead column on this side of array# 2, which prevents an accurate determination of the PSF peak position.

8.1 Straylight intensity

Internal straylight could in principle be observed on any pair of arrays symmetrical with respect to the center of the focal plane. However, since arrays# 1 and 3 were not operational during the tests, our investigation of the straylight was restricted to the array pairs (2,5) and (4,7).

We stacked a large number of individual PSF images, for a total of 34 min of acquisition time, in order to obtain high S/N images. For each PSF position, we analyzed the image of the whole focal plane, and computed the contribution

Table 3 Elevation-averaged measurements of the focal plane geometry parameters. The vertical line separates arrays from the TRANS and REFLEX focal planes respectively.

Array	δ_x [′/pix]	δ_y [′/pix]	α [°]	x_0 [pix]	y_0 [pix]	δ^0_{cel} [pix]	δ^0_{el} [pix]
2	-1.462±0.027	1.463±0.030	-46.397±0.351	7.5	7.5	22.381±0.266	-5.350±0.269
6	-1.518±0.025	1.388±0.056	-43.300±0.349	7.5	7.5	-4.821±0.315	20.722±1.060
5	-1.478±0.021	1.452±0.048	-42.155±0.190	7.5	7.5	-22.765±0.268	2.208±0.998
4	1.511±0.037	1.397±0.042	44.351±0.249	7.5	7.5	-4.691±0.282	20.781±1.066
8	1.461±0.030	1.453±0.053	47.412±0.296	7.5	7.5	22.135±0.244	-6.033±0.252
7	1.501±0.025	1.485±0.027	46.231±0.232	7.5	7.5	3.466±0.375	-24.336±1.097

Table 4 Peak positions and intensity of the main collimator source and internal straylight. The intensities are derived using the amplitude or integrated intensity of a Gaussian fit.

	Array	position (x,y) [pixel]	position (cel,el) [′]	PSF amplitude [ADU]	PSF integral [ADU]
source	4	(11.9, 7.0)	(-0.43, 15.8)	18.5	5418.3
straylight	7	(4.7, 7.6)	(0.67, -21.3)	0.0378	84.8
ratio				0.20%	1.5%

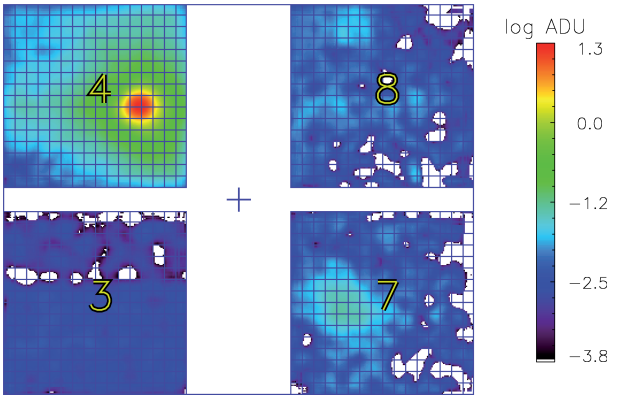

Fig. 19 Image in log scale of the brightness distribution across the focal plane when the collimator source is positioned on array# 4. Faint internal straylight can be seen on array# 7, at a position symmetrical to the source with respect to the optical axis.

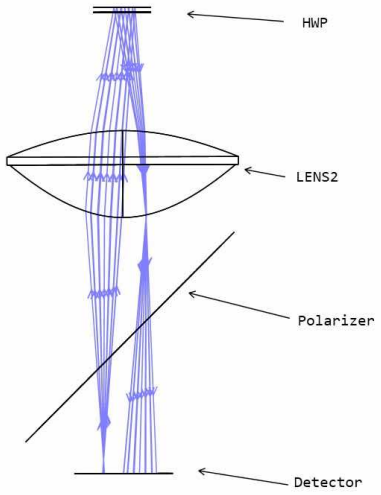

Fig. 20 Schematic view illustrating the possible origin of the internal straylight as simulated using the Zemax software. Light reflected off the detector is reflected by the HWP back to the detector.

from straylight. Figure 19 shows the intensity distribution on the TRANS array, when the collimator source was centered at a given location on array# 4. The image is shown in log scale to emphasize the detailed structure of faint signal. The straylight can be seen as an extended patch on array# 7, symmetrical to the main source with respect to the focal plane center.

Table 4 gives the intensity of the source and of the corresponding straylight. For the pair shown in Fig. 19, the straylight peak amplitude is $\sim 0.2\%$ of the source PSF peak, and the total straylight intensity is $\sim 0.6\%$ of the total source PSF intensity, taking into account the contribution from the source PSF at the location of the straylight.

8.2 Origin of the straylight

We performed a simulation of the straylight using the Zemax software. Reflectivity FTS measurements performed on the arrays indicate that, in the 240 μm band, $\simeq 8\%$ of the incident light is reflected off the focal plane and can propagate through the optical system as shown in Fig. 20. The simulation used the configuration described in Sect. 8.1 with the source located at pixel (11.8, 7.0) of array# 4. Taking into account the measured reflectivity of the detectors in the 240 μm band of $\simeq 8\%$ (absorptivity of 0.92), the transmission of the band-pass filter in front of the detector (transmission of 0.52), the off-axis transmission of lens lens L2 (transmission: 0.35) and assuming a reflectivity of the HWP

of 0.28, the straylight intensity is predicted to be $\simeq 0.3\%$ of the total source intensity. This value is compatible with the range of measured values given in Tab. 4, owing to the large uncertainties on the input optical transmissions and on the measurements. We conclude that the straylight is most likely due to light reflected by the detectors and reflected back by the HWP of the instrument, due to impedance mismatch within the plate stack.

9 Conclusions

We have performed end-to-end ground calibration test for the *PILOT* balloon-borne experiment. These tests have allowed us to evaluate the quality of the *PILOT* optics. The results obtained will play an important role in the analysis of the *PILOT* in-flight data. Our results can be summarized as follows:

- The spatial distribution of the background on the focal plane is determined by the transmission of the optics, in particular lens L2.
- The background level during ground tests was about 4 pW/pix, which is in the appropriate range for the bolometers.
- The spatial shape of the background polarization angle ψ is similar for the TRANS and REFLEX arrays. The angle ψ is distributed between -60° and -20° . The polarization fraction p is distributed between 0 % and 7 %.
- The ICS produces sufficient signal for efficient in-flight calibration while remaining well below the background level and therefore not changing the operating point of bolometers.
- We determined the best focus position for M1 and measured the tolerance of the focus position. These tests showed that the focus requirement can be relaxed by a factor of about two.
- At the best focus position, the measured PSF FWHM is about $2'$ which is consistent with a diffraction-limited PSF.
- We derived the geometry of the focal plane with good accuracy.
- We showed that the flexion of the mechanical system for elevations ranging between 20° and 50° is less than $1'$.
- We detect faint internal straylight when observing strong point sources, that is consistent with a reflection by the HWP.

The polarization of the background signal should have little to no impact on the measurements with *PILOT*, since we do not rotate the HWP during individual sky observations, and an arbitrary zero-level is to be subtracted from each scan in anycase, to remove contribution from the residual atmosphere and the instrument. The observed quality of the PSF indicate good optical performances, which should be easy to reproduce in flight, given that the sensitivity to defocus is less critical than initially expected. This will be check on calibration point sources during flight. The accuracy of focal plane geometry and its possible variations with elevation should be sufficient for first order map making reconstruction. However, additional pointing check on bright sources will probably be necessary to match the pointing reconstruction accuracy of the stellar sensor. The observed internal straylight level indicates that specific data processing may be required to observed faint polarization signal near strong astronomical sources.

Acknowledgements *PILOT* is an international project that involves several European institutes. The institutes that have contributed to hardware developments for *PILOT* are IRAP and CNES in Toulouse (France), IAS in Orsay (France), CEA in Saclay (France), Sapienza University in Rome (Italy) and Cardiff University (UK). This work was supported by the CNES. It is based on instrumentation work preparatory to the *PILOT* mission, which has been flown under a balloon operated by CNES and CSA , under the agreement between CNES and CNRS /INSU, during the Timmins 2015 campaign.

References

1. K. Foyle, C.D. Wilson, E. Mentuch, G. Bendo, A. Dariush, T. Parkin, M. Pohlen, M. Sauvage, M.W.L. Smith, H. Roussel, M. Baes, M. Boquien, A. Boselli, D.L. Clements, A. Cooray, J.I. Davies, S.A. Eales, S. Madden, M.J. Page, L. Spinoglio, MNRAS**421**, 2917 (2012). DOI 10.1111/j.1365-2966.2012.20520.x
2. F. Combes, M. Boquien, C. Kramer, E.M. Xilouris, F. Bertoldi, J. Braine, C. Buchbender, D. Calzetti, P. Gratier, F. Israel, B. Koribalski, S. Lord, G. Quintana-Lacaci, M. Relaño, M. Röllig, G. Stacey, F.S. Tabatabaei, R.P.J. Tilanus, F. van der Tak, P. van der Werf, S. Verley, A&A**539**, A67 (2012). DOI 10.1051/0004-6361/201118282
3. T. Hill, P. André, D. Arzoumanian, F. Motte, V. Minier, A. Men'shchikov, P. Didelon, M. Hennemann, V. Könyves, Q. Nguyen-Luong, P. Palmeirim, N. Peretto, N. Schneider, S. Bontemps, F. Louvet, D. Elia, T. Giannini, V. Revéret, J. Le Pennec, L. Rodriguez, O. Boulade, E. Doumayrou, D. Dubreuil, P. Gallais, M. Lortholary, J. Martignac, M. Talvard, C. De Breuck, A&A**548**, L6 (2012). DOI 10.1051/0004-6361/201220504
4. N. Scoville, K. Sheth, H. Aussel, P. Vanden Bout, P. Capak, A. Bongiorno, C.M. Casey, L. Murchikova, J. Koda, J. Álvarez-Márquez, N. Lee, C. Laigle, H.J. McCracken, O. Ilbert, A. Pope, D. Sanders, J. Chu, S. Toft, R.J. Ivison, S. Manohar, ApJ**820**, 83 (2016). DOI 10.3847/0004-637X/820/2/83
5. F. Boulanger, A. Abergel, J.P. Bernard, W.B. Burton, F.X. Desert, D. Hartmann, G. Lagache, J.L. Puget, A&A**312**, 256 (1996)
6. G.L. Pilbratt, J.R. Riedinger, T. Passvogel, G. Crone, D. Doyle, U. Gageur, A.M. Heras, C. Jewell, L. Metcalfe, S. Ott, M. Schmidt, A&A**518**, L1 (2010). DOI 10.1051/0004-6361/201014759
7. J.A. Tauber, N. Mandolesi, J.L. Puget, T. Banos, M. Bersanelli, F.R. Bouchet, R.C. Butler, J. Charra, G. Crone, J. Dodsworth, et al., A&A**520**, A1 (2010). DOI 10.1051/0004-6361/200912983
8. J.L. Dotson, J. Davidson, C.D. Dowell, D.A. Schleuning, R.H. Hildebrand, ApJS**128**, 335 (2000). DOI 10.1086/313384
9. N. Ponthieu, J.F. Macías-Pérez, M. Tristram, P. Ade, A. Amblard, R. Ansari, J. Aumont, É. Aubourg, A. Benoît, J.P. Bernard, A. Blanchard, J.J. Bock, F.R. Bouchet, A. Bourrachot, P. Camus, J.F. Cardoso, F. Couchot, P. de Bernardis, J. Delabrouille, F.X.

Désert, M. Douspis, L. Dumoulin, P. Filliatre, P. Fosalba, M. Giard, Y. Giraud-Héraud, R. Gispert, J. Grain, L. Guglielmi, J.C. Hamilton, S. Hanany, S. Henrot-Versillé, J. Kaplan, G. Lagache, A.E. Lange, K. Madet, B. Maffei, S. Masi, F. Mayet, F. Nati, G. Patanchon, O. Perdereau, S. Plaszczynski, M. Piat, S. Prunet, J.L. Puget, C. Renault, C. Rosset, D. Santos, D. Vibert, D. Yvon, A&A**444**, 327 (2005). DOI 10.1051/0004-6361:20052715

10. Planck Collaboration, P.A.R. Ade, N. Aghanim, D. Alina, M.I.R. Alves, C. Armitage-Caplan, M. Arnaud, D. Arzoumanian, M. Ashdown, F. Atrio-Barandela, et al., A&A**576**, A104 (2015). DOI 10.1051/0004-6361/201424082
11. J.P. Bernard, et al., Pilot: a balloon-borne experiment to measure the polarized fir emission of dust grains in the interstellar medium (2016). Submitted
12. C. Engel, I. Ristorcelli, J.P. Bernard, Y. Longval, C. Marty, B. Mot, G. Otrio, G. Roudil, Experimental Astronomy **36**, 21 (2013). DOI 10.1007/s10686-013-9332-7
13. C. Engel, et al., Optical design of the pilot balloon borne experiment: performances and tolerances (2016). In prep.
14. F. Simoens, P. Agnese, A. Beguin, J. Carcey, J.C. Cigna, J.L. Pornin, P. Rey, A. Vandeneynde, L. Rodriguez, O. Boulade, J. Lepennec, J. Martignac, E. Doumayrou, V. Reveret, L. Vigroux, in Millimeter and Submillimeter Detectors for Astronomy II, vol. 5498 (2004), vol. 5498, p. 177. DOI 10.1117/12.551299. URL http://dx.doi.org/10.1117/12.551299
15. G. Savini, P.A.R. Ade, J. House, G. Pisano, V. Haynes, P. Bastien, Appl. Opt. **48**(11), 2006 (2009). DOI 10.1364/AO.48.002006. URL http://ao.osa.org/abstract.cfm?URI=ao-48-11-2006
16. J.R. Pardo, J. Cernicharo, E. Serabyn, IEEE Transactions on Antennas and Propagation **49**(12), 1683 (2001). DOI 10.1109/8.982447
17. V. Buttice, F. Pajot, J.P. Bernard, M. Bouzit, A. Caillat, B. Crane, M. Chaigneau, J.P. Dubois, B. Leriche, Y. Longval, C. Marty, (2012), vol. 8452, pp. 84,520U–84,520U–6. DOI 10.1117/12.925187. URL http://dx.doi.org/10.1117/12.925187